

Bayesian learning of visual chunks by human observers

Gergő Orbán^{*†}, József Fiser[†], Richard N. Aslin[‡], and Máté Lengyel^{*§¶||}

^{*}Collegium Budapest Institute for Advanced Study, 2 Szentháromság utca, Budapest H-1014, Hungary; [†]Department of Psychology and Volen Center for Complex Systems, Brandeis University, 415 South Street, Waltham, MA 02454; [‡]Department of Brain and Cognitive Sciences, Center for Visual Science, Meliora 406, University of Rochester, Rochester, NY 14627; [§]Gatsby Computational Neuroscience Unit, University College London, Alexandra House, 17 Queen Square, London WC1N 3AR, United Kingdom; and [¶]Computational and Biological Learning Laboratory, Department of Engineering, University of Cambridge, Trumpington Street, Cambridge CB2 1PZ, United Kingdom

Edited by James L. McClelland, Stanford University, Stanford, CA, and approved December 28, 2007 (received for review September 5, 2007)

Efficient and versatile processing of any hierarchically structured information requires a learning mechanism that combines lower-level features into higher-level chunks. We investigated this chunking mechanism in humans with a visual pattern-learning paradigm. We developed an ideal learner based on Bayesian model comparison that extracts and stores only those chunks of information that are minimally sufficient to encode a set of visual scenes. Our ideal Bayesian chunk learner not only reproduced the results of a large set of previous empirical findings in the domain of human pattern learning but also made a key prediction that we confirmed experimentally. In accordance with Bayesian learning but contrary to associative learning, human performance was well above chance when pair-wise statistics in the exemplars contained no relevant information. Thus, humans extract chunks from complex visual patterns by generating accurate yet economical representations and not by encoding the full correlational structure of the input.

Bayesian inference | probabilistic modeling | vision

One of the most perplexing problems facing a human learner, in domains as diverse as natural language acquisition or visual object recognition, is representing in memory the rich and hierarchically structured information present in almost every aspect of our environment (1, 2). At the core of this problem lies the task of discovering how the building blocks of a hierarchy at one level, such as words or visual chunks, are constructed from lower-level features, such as syllables or line segments (3, 4). For example, in the domain of vision, many efficient object recognition systems, both natural (5) and artificial (6), use small visual fragments (chunks) to match the parts of an image. Successful recognition of objects in these systems depends crucially on determining which parts of the image match which chunks of the prespecified inventory. However, extracting chunks from the visual input for the construction of a proper inventory entails a fundamental challenge: in any single visual scene, there are multiple objects present, often without clear segregation because of partial occlusion, clutter, and noise, and so chunks cannot be identified just by relying on low-level grouping cues. Identical arguments have been made about the challenges inherent in identifying the “chunks of language,” words, from continuous speech streams in which low-level auditory grouping cues are known to be ambiguous with respect to word boundaries (7). Therefore, to resolve the ambiguity of chunks in any single scene, or sentence, an observer needs to learn about chunks across multiple visual scenes, or sentences, and to identify chunks as consistently reappearing fragments.

Classic studies of chunking in human long-term memory revealed a variety of explicit strategies, such as verbal cue formation with highly familiar facts in a given domain (8, 9), to reduce the amount of newly stored information. However, chunking at the level of perception requires an inventory that is learned implicitly by a mechanism that is available even to infants. Within the domain of implicit chunk learning, there is substantial controversy about whether chunk learning is based

on abstract rule-based operations on lower-level features or relies on associative learning of their cooccurrence statistics (10, 11). Here, we show that such implicit chunk learning cannot be explained by simple correlation-based associative learning mechanisms; rather, its characteristics can be both qualitatively and quantitatively predicted by a Bayesian chunk learner (BCL). The BCL forms chunks in a statistically principled way, without any strong prior knowledge of the possible rules for their construction, thus bridging the gap between low-level statistics and abstract rules.

Past attempts to study the learning of statistics and rules have been conducted in domains such as artificial grammar learning (12, 13), serial reaction times (14, 15), word segmentation from fluent speech (16, 17), and pattern abstraction from strings of words (18, 19). In contrast, we focus on pattern learning from multielement visual scenes (Fig. 1), because a number of subtle structural manipulations that could tease apart competing models of implicit learning have recently been conducted with such stimuli using a well controlled paradigm (20–22). We exploit this paradigm by fitting past data to the BCL and then generating a key prediction from the BCL that we test empirically in a study of human performance.

In our visual pattern-learning paradigm, we used “combos,” combinations of shapes, as the building blocks of a series of multielement familiarization scenes (see Fig. 1 and *Methods*). Just as any single natural scene is formed by multiple objects or other coherent chunks, with the same object or chunk being present in several scenes, there were multiple combos shown in each familiarization scene, with the same combo reappearing across multiple scenes. Importantly, neither the human participants nor the BCL was provided with any strong low-level grouping cues identifying combos or any information about the underlying structural rules by which the visual scenes were constructed from these combos. Thus, this paradigm left statistical contingencies among the recurring shapes in the familiarization scenes as the only available cues reliably identifying individual chunks; learning was unsupervised and based entirely on mere observation of exemplars.

When learning must proceed without supervision, as in our experimental paradigm, a natural objective is that the learner should develop a faithful internal model of the environment (23). A model of the environment in our task can be formalized as a probability distribution over all possible sets of visual scenes, and

Author contributions: G.O., J.F., and M.L. designed research; G.O., J.F., and R.N.A. performed research; G.O., J.F., and M.L. analyzed data; and G.O., J.F., R.N.A., and M.L. wrote the paper.

The authors declare no conflict of interest.

This article is a PNAS Direct Submission.

||To whom correspondence should be addressed. E-mail: lmate@gatsby.ucl.ac.uk.

This article contains supporting information online at www.pnas.org/cgi/content/full/0708424105/DC1.

© 2008 by The National Academy of Sciences of the USA

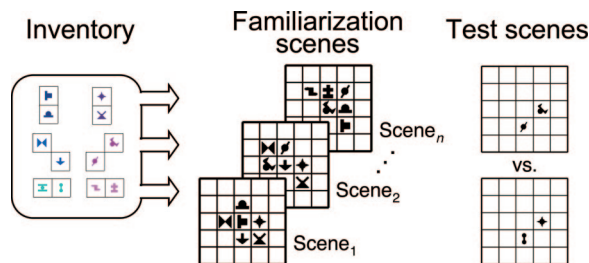


Fig. 1. Experimental design. Schematic of scene generation in the experiments. Shapes from the inventory (Left) were organized into combos (pairs in this example). The spatial arrangement of the shapes within each combo was fixed across all scenes. For each familiarization scene, combos were pseudo-randomly selected from this inventory and placed in adjacent positions within a rectangular grid (Center). Scenes were presented once every 2 sec during familiarization. The test phase consisted of 2AFC trials in which each of two scenes (Right) depicted a subset of shapes from the familiarization scenes. One subset was a true combo from the inventory (or a part thereof, called an embedded combo) and the other subset consisted of shapes from two different combos (a mixture combo).

the faithfulness of a model is expressed by the probability it assigns to the particular set of scenes shown in the familiarization phase. In the case of chunk learning, each inventory of chunks specifies a different distribution over scenes

$$P(\text{scene}_1, \text{scene}_2, \dots, \text{scene}_n | \text{inventory}), \quad [1]$$

The probability this distribution assigns to the set of familiarization scenes is called the likelihood of the inventory. Intuitively, the likelihood of an inventory quantifies how easy or difficult it is to piece together all previously attested visual scenes from its constituent chunks (see *Methods*).

Crucially, more complex inventories of chunks can generate a larger variety of possible scenes. However, because the probabilities that an inventory assigns to sets of scenes in Eq. 1 must sum to exactly 1.0, the probability value assigned to each possible set of scenes will be smaller on average for more complex inventories. This self-normalizing effect is known as the “automatic Occam’s razor” property of Bayesian model comparison (24). Because of the automatic Occam’s razor effect, if an inventory is too complex, its likelihood will be small, because it distributed most of its probability mass over too many other sets of scenes. Similarly, if the inventory is too simple, its likelihood will be small again, because it cannot account for all of the details of the familiarization scenes. The likelihood will be high only for an inventory whose complexity is “just right” for the given set of familiarization scenes. Thus, according to Bayesian model comparison, the optimal inventory is the one complex enough to capture previous visual experience sufficiently well but that does not over-fit the input data, which would prevent generalization to novel scenes.

For the construction of the BCL, we formalized the notion of a “chunk” as a hidden (or latent) variable that captures essential information about the presence and location of a number of shapes in the familiarization scenes. The BCL assumes that if a chunk is present in a scene, the probability that the shapes contained in that chunk are present in a particular spatial configuration in the scene is increased. If the chunk is absent from the scene, then each of the shapes contained within it have a fractional chance of appearing “spontaneously,” independently of the other shapes. Thus, although only the shapes themselves can be observed directly, chunks can be inferred as suspicious coincidences of particular shape configurations (25). This allows for computing the probability of familiarization scenes for any particular inventory (Eq. 1). Finally, the BCL applies Bayesian model comparison to compare the viability of

different inventories and to prefer the one with optimal complexity [see *Methods* and [supporting information \(SI\) Appendix, SI Text](#), and [SI Tables 1–3](#), for further details].

Learning about chunks is but one way of forming a model of the environment, so we compared the BCL to four alternative computational models to rule out the possibility that participants used some simpler but less-optimal learning strategy. These alternative models embody the most often invoked mechanisms by which humans could learn about visual scenes or auditory sequences (26). The first two were sophisticated counting mechanisms, at the level of both individual shape frequencies and cooccurrence frequencies of shapes (see [SI Appendix, SI Text](#)). These models are typical of approaches that treat human learning as storing the averaged sum of episodic memory traces. The third model computes conditional probabilities (cooccurrence frequencies normalized by individual shape frequencies) of all possible shape pairs (see [SI Appendix, SI Text](#)). It is the most widely accepted account of human performance in statistical learning experiments in visual and auditory domains (16, 17, 20). The fourth model, the associative learner (AL), is a statistically optimal implementation of widely recognized associative learning mechanisms (27, 28). It uses a probabilistic mechanism, much like the BCL, but it keeps track of all pair-wise correlations between shapes without an explicit notion of chunks (see *Methods*). Here, we focus on the comparison between the AL and the BCL, because the first three models failed to capture one or more key patterns of human performance in our visual pattern-learning paradigm. For a comparison of all five models, see [SI Appendix, SI Text](#), [SI Table 4](#), and [SI Fig. 4](#).

Results

To determine whether human performance is best described by the AL or the BCL, we compared the behavior of these models to the results of previously published experiments of chunk formation by humans (20, 22). These experiments provided some well quantified results that were inexplicable from the perspective of the three simpler learning models and thus established an appropriate test bed for assessing any viable theory of chunk formation (Fig. 2). The first set of these experiments showed that humans automatically extract the true pair combos from the familiarization scenes under various conditions, even when the cooccurrence frequencies of shapes bear no information about the identities of chunks (Fig. 2*A* and *B*). These results confirmed that humans could, in principle, learn higher-order visual chunks as a part of their internal inventory. Both the AL and the BCL models could reproduce these results.

In a second set of experiments, combos with more than two shapes (triplets or quadruples) were used to create larger coherent structures to test how humans learn hierarchically structured information (Fig. 2*C* and *D*). Just as with pairs, humans readily distinguished between these more extensive combos and random combinations of shapes. However, they produced disparate results when comparing smaller part combos (pairs or triplets), embedded in one of the true combos, with mixture combos of the same size (composed of shapes belonging to different true combos). They did not distinguish between pairs embedded in true triplets (Fig. 2*C*) or quadruples (Fig. 2*D*) from mixture pairs but could still distinguish triplets embedded in true quadruples from mixture triplets (Fig. 2*D*). These results provided evidence that humans might selectively encode particular chunks while neglecting some others, depending on the hierarchical relation between the chunks. Earlier theoretical accounts of learning, captured by the three simpler models, could predict only identical performance on all test types in these experiments (see [SI Appendix, SI Text](#), and [SI Fig. 4](#)). In contrast, both the BCL and the AL reproduced all of these results by predicting chance performance with embedded pairs and a general trend

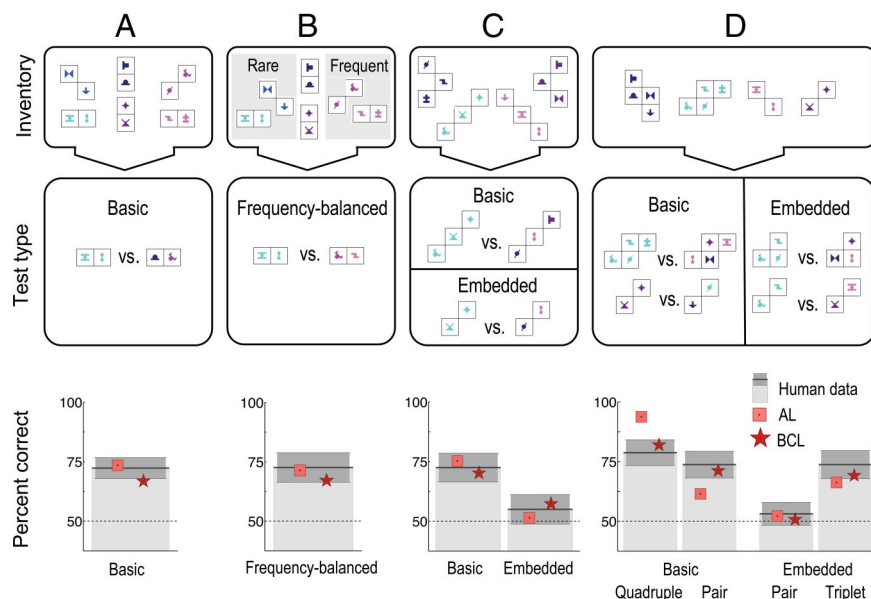


Fig. 2. Summary of experimental manipulations [inventories (Top) and test types (Middle)], and discrimination performance (Bottom) of human participants (gray bars with dark shading indicating standard error of the mean, SEM). The predictions of the AL (pink squares) and the BCL (red stars) are shown for a series of experiments from refs 20 and 22 using increasingly complex inventories. (Colors were not included in the actual shapes seen by participants.) For a stringent comparison, the parameters of the AL were adjusted independently for each experiment to obtain best fits, whereas the BCL used a single parameter optimization across all experiments. (A) Inventory containing six equal-frequency pairs. Human performance was above chance on the basic test of true pairs vs. mixture pairs. (B) Inventory containing six pairs of varying frequency. Human performance was above chance on the test of true rare pairs vs. frequency-balanced mixture pairs. (C) Inventory containing four equal-frequency triplets. Human performance was above chance on the basic test of true triplets vs. mixture triplets and at chance on the test of embedded pairs vs. mixture pairs. (D) Inventory containing two quadruples and two pairs, all with equal frequency. Human performance was above chance on the basic tests of true quadruples or pairs vs. mixture quadruples or pairs, and on the test of embedded triplets vs. mixture triplets, but it was at chance on the test of embedded pairs vs. mixture pairs. Both models captured the overall pattern of human performance in all these experiments.

for larger embedded combos to be increasingly better recognized (*SI Appendix*, *SI Text*, and *SI Figs. 4–6*).

Taken together, these experiments could rule out the three simpler models as viable accounts of human visual learning, but they were insufficient to distinguish between the AL and the BCL. Although the BCL provided a substantially better quantitative fit to these data than the AL (BCL: $r = 0.88$, $P < 0.0002$; AL: $r = 0.74$, $P < 0.01$, across $n = 12$ different tests; see also *SI Appendix*, *SI Figs. 5A and 6*), there was no strong qualitative difference between them in predicting human behavior in these experiments.

To be able to make a qualitative distinction between the BCL and the AL, we capitalized on a crucial prediction that the BCL made and that stood in stark contrast with that derived from conventionally accepted theories, which assume that learning proceeds by computing pair-wise associations between elements (AL). The BCL, but not the AL, should be able to extract the constituent chunks of visual scenes even if pair-wise statistics between shapes contain no relevant information about chunk identity. To test this prediction, we designed an experiment that contained two groups of four shapes in which both the first- and second-order statistics between shapes were made identical (Fig. 3A). However, the shapes in one of the groups were always shown as triplet combos, whereas the shapes in the other group were shown individually (and occasionally all four of them were presented together). Consistent with the BCL, humans successfully learned to distinguish between triplets constructed from the elements of the two groups, whereas the AL was not able to make this distinction (Fig. 3B; see also *SI Appendix*, *SI Figs. 5 and 6*). Specifically, although both the BCL and the AL recognized triplets from the first group of four against mixture triplets (Fig. 3B Left), the AL, but not the BCL, also falsely recognized triplets from the second group of four (Fig. 3B Center), and the BCL but not the AL distinguished between triplets from the two groups in a direct comparison (Fig. 3B Right). This double dissociation

between the BCL and the AL was also reflected in their ability to predict human performance levels in the last experiment after fitting them to all previous data (BCL: $r = 0.92$, $P < 0.006$; AL: $r = -0.23$, $P > 0.65$, across the $n = 4$ new test conditions; see also *SI Appendix*, *SI Figs. 5A and 6*). Thus, not only does the BCL capture human performance qualitatively better than the AL, but also it does so with a parameter-free fit of the empirical data from our final experiment.

Discussion

The present series of computational analyses and empirical findings extend previous Bayesian ideal observer analyses (29, 30) that have provided valuable insights into sensory and perceptual processing, to the domain of learning at the level of perception. Earlier work has demonstrated that humans are adapted to the environmental statistics, and they draw near-optimal perceptual inferences when faced with internal or external sources of uncertainty (31–34). However, because the learning demands of these studies were limited, the optimality of the learning process itself in such perceptual domains has not previously been addressed. Our results suggest that human chunk learning is remarkably close to optimal, especially given that participants did not become consciously aware of the existence of the combos, let alone their identities.

Our results also have implications for the distinction between statistical and rule learning. Statistical learning has been characterized as focusing on transitional or conditional probabilities that can be used to extract segments and simple chunks from the input (26) but are insufficient for learning more complex structures. In contrast, rule learning has been postulated as a qualitatively different mechanism that can capture abstract structural properties of the input that are inaccessible to any statistical learning mechanism (10, 19). Although particular details of the BCL were clearly motivated by the specific visual

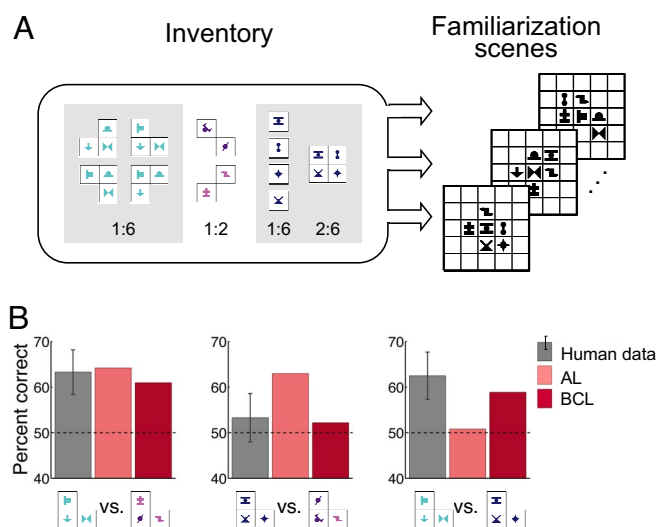


Fig. 3. Correlation-balanced experiment contrasting the BCL and the AL. (A) The inventory of shapes and their rules of combination. The inventory consisted of two groups of four shapes (shaded boxes), and two pairs. Shapes in the first group of 4 were always shown as one of four triplets sharing the same four shapes; shapes in the other group of 4 were shown either as single shapes or sometimes as a quadruple. The numbers below each subset of combos indicates their ratio of presentation across the entire familiarization phase. Shapes in the two groups of 4 had the same occurrence frequencies (1/2) and within-group correlations (1/3). The familiarization scenes were composed and presented the same way as in all prior experiments. (B) The three tests used to assess human performance and the actual performance (gray bars with error bars indicating SEM) along with predictions of the AL (pink bars) and the BCL (red bars). One test contrasted true triplets from the first group of 4 with mixture triplets: human performance was above chance ($P < 0.017$) and was predicted by both models (Left). The second test contrasted triplets constructed from the shapes of the second group of 4 ("false" triplets) with mixture triplets: human performance was not above chance ($P > 0.24$), and only the BCL predicted this result (Center). The final test contrasted true with false triplets: human performance was above chance ($P < 0.0001$), and again only the BCL predicted this result (Right). Significance was assessed by two-tailed Student's t tests.

pattern-learning experiments we used to test our theory or by mathematical tractability, we expect its two fundamental computational principles have domain-general significance: formulating chunks as hidden variables of the environment and using Bayesian model comparison to select from alternative inventories of chunks. Thus, our results raise the possibility that, for the formation of chunks even outside the domain of vision, rule learning is merely a higher-order example of extracting hidden variables (latent structures) from a complex set of inputs in a way close to being statistically optimal. As a result, the distinction between statistical and rule learning disappears when both are considered from the perspective of Bayesian model comparison.

Bayesian model comparison, entailing the automatic Occam's razor effect, and related statistical techniques have been applied with great success to understanding various forms of learning structured information, ranging from classical conditioning in animals (35) to high-level cognitive domains in humans, such as causal induction (36), semantic representations (37), and word learning (38). Despite substantial theoretical work exploring how networks of neurons can perform at least approximate Bayes-optimal inference (39), it is still an open issue how the nervous system performs such highly complex computations efficiently in a wide variety of domains and at a number of levels of information abstraction. Establishing a formal theory of chunk learning sets the stage for subsequent algorithms that implement an ideal learner in a neurally plausible manner.

Methods

Human Experiments. Participants were familiarized with a series of scenes composed of 12 moderately complex filled black shapes on a white background (Fig. 1). The assignment of the 12 shapes to combos was randomized across participants to control for effects due to specific shape configurations. For the construction of each scene, two or three pseudorandomly chosen combos were placed within a 3×3 or 5×5 rectangular grid. To ensure there were no obvious spatial cues identifying the combos, the positions of the combos within the grid were randomized with the constraint that at least one shape in a combo had to occupy a grid location adjacent to one shape in another combo. Across the various experiments, these constraints generated a set of 144–212 possible scenes. These scenes were presented one at a time for 2 sec, with 1-sec pauses between them, and each participant was instructed to simply view the scenes without any explicit task.

In each two-alternative forced choice (2AFC) trial of the test phase, participants were presented with two partial scenes, with the shapes approximately centered in the grid, and they selected by key press (1 or 2) the test scene more familiar based on the scenes viewed during familiarization. The two test scenes of each trial were composed according to the rules described in Fig. 2 Middle. During familiarization, participants never saw a spatially separated combo by itself, thus correct responding in the test required generalization from what had been previously seen. The order of the two test scenes in a trial was counterbalanced for each participant's test phase, and the presentation order of the test trials was individually randomized. Each test display was presented for 2 sec with a 1-sec pause between them.

Undergraduates from the University of Rochester or Brandeis University, ranging in age from 18 to 25 years, served as the participants and were paid \$10 per session. There were 20–32 participants in each of the experiments. All participants were naïve with respect to the purpose of the experiment and participated only in one experiment. After the test phase was completed, participants were debriefed to determine their awareness of the underlying chunks. There was no consistent evidence in their verbal reports that the participants became aware of the underlying structure, and their confidence did not correlate with their performance in the test trials. Familiarization and test scenes were presented on a 21-in Sony Trinitron 500PS monitor at $1,024 \times 728$ resolution from a 1-m viewing distance. The extent of the 5×5 grid was 11.4° , and the maximum size of each shape was 1.14° . Stimuli were controlled by a Macintosh G4 or iMac computer by using MATLAB (Mathworks, Cambridge, U.K.) and the Psychophysics Toolbox (40). Two-tailed Student's t tests were used for assessing significance ($P < 0.05$) in all experiments.

All human experiments were conducted in accordance to University of Rochester or Brandeis University rules. Informed consent was obtained from all participants after the nature and possible consequences of the studies were explained. Experimental data shown in Fig. 2 and SI Appendix, SI Fig. 4 have been published (20, 22).

BCL. The BCL represents displayed scenes with two sets of variables: observed variables corresponding to the directly observable shapes (their presence or absence encoded by binary variables y_i , and their positions encoded by 2D vectors v_i) and hidden variables, or chunks, which are revealed to the observer only indirectly through their influences on the observed shapes (their presence or absence encoded by binary variables x_i and their positions encoded by 2D vectors u_i). An inventory of chunks (I) specifies the number of hidden variables and, for each hidden variable, the observed shapes it influences. For each inventory, additional parameters (θ) quantify the magnitude of these influences (see also SI Appendix, SI Text). The task of the BCL is to infer the probability of alternative inventories after seeing the familiarization scenes.

Statistical inference requires an explicit probabilistic model of how scenes are generated. According to the generative model used by the BCL, hidden variables (chunks) appear independently from each other in each scene:

$$\begin{aligned} P(x, u | \theta, I) &= \prod_i P(x_i, u_i | \theta, I) \\ &= \prod_i \text{Bernoulli}(x_i; \text{Sigmoid}(w_{x_i})) \\ &\quad \cdot [\text{Normal}(u_i; c_{x_i}, \sigma_{x_i}^2 \cdot \mathbf{I})]^{x_i}, \end{aligned} \quad [2]$$

where w_{x_i} and c_{x_i} parameterize the appearance probability x_i and preferred spatial position u_i of chunk i , and $\sigma_{x_i}^2$ is its spatial variance around the preferred position, with \mathbf{I} being the (2×2) identity matrix. (SI Appendix, SI Table 1 gives definitions of nonstandard function names used in equations throughout the text.)

Given a configuration of chunks, the appearances of shapes are independent:

$$P(y, v|x, u, \theta_I, I) = \prod_j P(y_j, v_j|x, u, \theta_I, I) = \prod_j \text{Bernoulli}\left(y_j; \text{Sigmoid}\left(w_{y_j} + \sum_{i \in \text{par}_I(j)} x_i w_{ij}\right)\right) \cdot \left(\frac{1}{Z} \text{Normal}(v_j; c_{y_j}, \sigma_{y_j}^2) \prod_{i \in \text{par}_I(j)} (\text{Normal}(v_j; u_i + c_{ij}, \sigma_{ij}^2))^{x_i}\right)^{y_j}, \quad [3]$$

where for each observed variable j , $\text{par}_I(j)$ is the collection of hidden variables that influence it according to inventory I , matrix element w_{ij} quantifies the amount of influence that the presence of chunk x_i has on its presence y_j , matrix element c_{ij} is its preferred relative position from the center of mass of chunk u_i , w_{y_j} and c_{y_j} give its spontaneous appearance probability and absolute position in the absence of the chunks in $\text{par}_I(j)$ (i.e., when its appearance is due to noise), σ_{ij}^2 and $\sigma_{y_j}^2$ are the spatial variances around the respective preferred positions, and Z is an appropriate normalizing constant.

Because presented scenes specify only the appearances of the observed variables, the predictive probability of a scene is computed from Eq. 3 and by marginalizing over the values of hidden variables:

$$P(y, v|\theta_I, I) = \sum_x \int du P(y, v|x, u, \theta_I, I) P(x, u|\theta_I, I). \quad [4]$$

Familiarization scenes, collectively constituting training data (\mathcal{D}) for the learner, are assumed to be independent and identically distributed, thus the likelihood of an inventory with its parameters is obtained by a product of the individual predictive probabilities:

$$P(\mathcal{D}|\theta_I, I) = \prod_t P(y^{(t)}, v^{(t)}|\theta_I, I), \quad [5]$$

where $y^{(t)}, v^{(t)}$ are the appearances of shapes in scene t .

The marginal likelihood of an inventory (Eq. 1), which is the source of the automatic Occam's Razor effect (24), is calculated by integrating out the parameters from the parameter-dependent likelihood (Eq. 5) using a prior over parameters (see *SI Appendix, SI Text and SI Table 2*):

$$P(\mathcal{D}|I) = \int d\theta_I P(\mathcal{D}|\theta_I, I) P(\theta_I|I). \quad [6]$$

According to Bayes' rule, this marginal likelihood is combined with a prior distribution over inventories (see *SI Appendix, SI Text and SI Table 2*) to yield a posterior distribution over inventories:

$$P(I|\mathcal{D}) = P(\mathcal{D}|I)P(I)/P(\mathcal{D}). \quad [7]$$

Given the posterior distribution, the predictive probability of test scene T is calculated by using again Eq. 3 and marginalizing over the posterior distribution of inventories and parameters:

$$P(T) = \sum_I \int d\theta_I P(y^{(T)}, v^{(T)}|\theta_I, I) P(\theta_I, I|\mathcal{D}), \quad [8]$$

where $P(\theta_I, I|\mathcal{D}) = P(\mathcal{D}|\theta_I, I)P(\theta_I|I)/P(\mathcal{D})$. Because the integral implied by Eq. 8 is analytically intractable, it was approximated by a sum over samples from the joint posterior of parameters and inventories, $P(\theta_I, I|\mathcal{D})$ (see *SI Appendix, SI Text*).

To provide test performances that were directly comparable to the results of the 2AFC test trials with humans, choice probability was computed as a softmax function of the log probability ratio of test scenes:

$$P(\text{choose } T_1) = \text{Sigmoid}[\beta \cdot \log(P(T_1)/P(T_2))], \quad [9]$$

where β was the only parameter in the BCL that was used to fit simulation results to human data. (This also ensured that strictly 50% choice probability was predicted for comparisons of equally familiar scenes whose log probability ratio was zero.) It was fitted to data from Experiments 1–4 (Fig. 2), and the β value thus obtained was then used to predict experimental percent correct values (using again Eq. 9) in the correlation-balanced experiment (Fig. 3). *SI Appendix, SI Fig. 5* shows the results of fitting and prediction. An earlier version of this model without a spatial component has been published (41).

AL. The AL followed a logic very similar to that of the BCL, except that rather than assuming chunks (hidden variables) to explain dependencies between shapes, it directly learned all pair-wise statistics between them. Therefore, its task was to infer a distribution over these statistics, θ (see *SI Appendix, SI Text and SI Table 3*). For this, Eqs. 2–4 were substituted with the following single equation:

$$P(y, v|\theta) = \frac{1}{Z} \exp\left(\frac{1}{2} \sum_{j,k \neq j} y_j y_k w_{jk} + \sum_j y_j w_{y_j}\right) \cdot \prod_{j,k \neq j} (\text{Normal}(v_j - v_k; c_{jk}, \sigma_{jk}^2))^{\frac{1}{2} y_j y_k} \prod_j (\text{Normal}(v_j; c_{y_j}, \sigma_{y_j}^2))^{y_j}, \quad [10]$$

where w_{y_j} and $w_{jk} = w_{kj}$ parameterize the occurrence and cooccurrence probabilities of shapes, just as in the Boltzmann machine (42), c_{y_j} and $c_{jk} = c_{kj}$ are the preferred positions and relative positions of shapes, $\sigma_{y_j}^2$ and $\sigma_{jk}^2 = \sigma_{kj}^2$ are the spatial variances around these preferred positions, and Z is the partition function ensuring that the distribution is properly normalized.

Again, β was the only parameter that was specifically tuned to fit experimental data. For Figs. 2 and 3, parameter β (see Eq. 9) was fitted for each experiment individually, except for the baseline and frequency-balanced experiments (Fig. 2 A and B) that were fitted together (so that there were at least two data points to be fitted in each case). To facilitate a direct comparison with the capacity of the BCL for matching human performance (*SI Appendix, SI Fig. 5*), *SI Appendix, SI Fig. 6* shows the results of fitting β with the same procedure as that used for the BCL (see also *SI Appendix, SI Text*).

ACKNOWLEDGMENTS. We thank Nathaniel Daw, Peter Dayan, and Eörs Szathmáry for discussion and Peter Dayan for comments on an earlier version of this manuscript. This work was supported by the European Union Framework 6 (Grant IST-FET 1940, G.O. and M.L.), the National Office for Research and Technology (Grant NAP2005/KCKHA005, to G.O. and M.L.), the Gatsby Charitable Foundation (M.L.), the Swartz Foundation (J.F. and G.O.), and the National Institutes of Health (Grant HD-37082, to R.N.A.).

- Harris ZS (1951) *Structural Linguistics* (Univ of Chicago Press, Chicago).
- Peissig JJ, Tarr MJ (2007) Visual object recognition: do we know more now than we did 20 years ago? *Annu Rev Psychol* 58:75–96.
- Chomsky N, Halle M (1968) *The Sound Pattern of English* (MIT Press, Cambridge, MA).
- Riesenhuber M, Poggio T (1999) Hierarchical models of object recognition in cortex. *Nat Neurosci* 2:1019–1025.
- Ullman S, Vidal-Naquet M, Sali E (2002) Visual features of intermediate complexity and their use in classification. *Nat Neurosci* 5:682–687.
- Sudderth EB, Torralba A, Freeman WT, Willsky AS (2006) in *Advances in Neural Information Processing Systems 18*, eds Weiss Y, Schölkopf B, Platt J (MIT Press, Cambridge, MA), pp 1297–1304.
- Christiansen MH, Allen J, Seidenberg MS (1998) Learning to segment speech using multiple cues: a connectionist model. *Lang Cognit Proc* 13:221–268.
- Halford GS, Cowan N, Andrews G (2007) Separating cognitive capacity from knowledge: a new hypothesis. *Trends Cognit Sci* 11:236–242.
- Miller GA (1956) The magical number seven plus or minus two: some limits on our capacity for processing information. *Psychol Rev* 63:81–97.
- Peña M, Bonatti LL, Nespor M, Mehler J (2002) Signal-driven computations in speech processing. *Science* 298:604–607.
- Seidenberg MS, MacDonald MC, Saffran JR (2002) Neuroscience. Does grammar start where statistics stop? *Science* 298:553–554.
- Reber AS (1967) Implicit learning of artificial grammars. *J Verb Learn Verb Behav* 6:855–863.
- Tunney RJ, Altmann GTM (1999) The transfer effect in artificial grammar learning: reappraising the evidence on the transfer of sequential dependencies. *J Exp Psych Learn Mem Cognit* 25:1322–1333.
- Cleeremans A, McClelland JL (1991) Learning the structure of event sequences. *J Exp Psychol Gen* 120:235–253.
- Shanks DR, Johnstone T (1998) in *Handbook of Implicit Learning*, eds Stadler MA, French PA (Sage, Thousand Oaks, CA), pp 533–572.

16. Newport EL, Aslin RN (2004) Learning at a distance I. Statistical learning of nonadjacent dependencies. *Cognit Psychol* 48:127–162.
17. Saffran JR, Newport EL, Aslin RN (1996) Word Segmentation: the role of distributional cues. *J Mem Lang* 35:606–621.
18. Gomez RL, Gerken LA (1999) Artificial grammar learning by 1-year-olds leads to specific and abstract knowledge. *Cognition* 70:109–135.
19. Marcus GF, Vijayan S, Bandi Rao S, Vishton PM (1999) Rule learning by seven-month-old infants. *Science* 283:77–80.
20. Fiser J, Aslin RN (2001) Unsupervised statistical learning of higher-order spatial structures from visual scenes. *Psychol Sci* 12:499–504.
21. Fiser J, Aslin RN (2002) Statistical learning of new visual feature combinations by infants. *Proc Natl Acad Sci USA* 99:15822–15826.
22. Fiser J, Aslin RN (2005) Statistical learning of higher-order temporal structure from visual shape sequences. *J Exp Psychol Gen* 134:521–537.
23. Dayan P, Abbott LF (2001) *Theoretical Neuroscience* (MIT Press, Cambridge, MA).
24. MacKay DJC (2003) *Information Theory, Inference, and Learning Algorithms* (Cambridge Univ Press, Cambridge, UK).
25. Barlow HB (1989) Unsupervised learning. *Neural Comp* 1:295–311.
26. Perruchet P, Pacton S (2006) Implicit learning and statistical learning: one phenomenon, two approaches. *Trends Cognit Sci* 10:233–238.
27. Gallistel CR (1990) *The Organization of Learning* (Bradford Books/MIT Press, Cambridge, MA).
28. Hebb DO (1949) *The Organization of Behavior* (Wiley, New York).
29. Kersten D, Mamassian P, Yuille A (2004) Object perception as Bayesian inference. *Annu Rev Psychol* 55:271–304.
30. Najemnik J, Geisler WS (2005) Optimal eye movement strategies in visual search. *Nature* 434:387–391.
31. Stocker AA, Simoncelli EP (2006) Noise characteristics and prior expectations in human visual speed perception. *Nat Neurosci* 9:578–585.
32. Ernst MO, Banks MS (2002) Humans integrate visual and haptic information in a statistically optimal fashion. *Nature* 415:429–433.
33. Körding KP, Wolpert DM (2004) Bayesian integration in sensorimotor learning. *Nature* 427:244–247.
34. Weiss Y, Simoncelli EP, Adelson EH (2002) Motion illusions as optimal percepts. *Nat Neurosci* 5:598–604.
35. Courville AC, Daw ND, Touretzky DS (2006) Bayesian theories of conditioning in a changing world. *Trends Cognit Sci* 10:294–300.
36. Griffiths TL, Tenenbaum JB (2005) Structure and strength in causal induction. *Cognit Psychol* 51:334–384.
37. Griffiths TL, Steyvers M, Tenenbaum JB (2007) Topics in semantic representation. *Psychol Rev* 114:211–244.
38. Xu F, Tenenbaum JB (2007) Word learning as Bayesian inference. *Psychol Rev* 114:245–272.
39. Pouget A, Dayan P, Zemel R (2000) Information processing with population codes. *Nat Rev Neurosci* 1:125–132.
40. Brainard DH (1997) The Psychophysics Toolbox. *Spatial Vision* 10:433–436.
41. Orbán G, Fiser J, Aslin RN, Lengyel M (2006) in *Advances in Neural Information Processing Systems 18*, eds Weiss Y, Schölkopf B, Platt J (MIT Press, Cambridge, MA), pp 1043–1050.
42. Hinton GE, Sejnowski TJ (1986) in *Parallel Distributed Processing: Explorations in the Microstructure of Cognition*, eds Rumelhart DE, McClelland JL (MIT Press, Cambridge, MA).

Supporting Text

Methods

Bayesian chunk learner (BCL)

Prior distributions An inventory I was defined as the set of chunks, and for each chunk the shapes it influenced (referred to as links). The prior probability of an inventory (used for computing the posterior over inventories in Eq. 7, and also used in Eq. 8) depended on the number of chunks H and the total number of links L :

$$\mathbb{P}(I) = \mathbb{P}(H) \mathbb{P}(L|H) \quad (\text{S1})$$

The prior distribution of the parameters of an inventory θ_I (used in Eqs. 6 and 8) included appearance probability parameters $W = \{w_{ij}, w_{x_i}, w_{y_j}\}$, and spatial position parameters $C = \{c_{ij}, c_{x_i}, c_{y_j}, \sigma_{ij}, \sigma_{x_i}, \sigma_{y_j}\}$:

$$\mathbb{P}(\theta_I|I) = \mathbb{P}(W|I) \mathbb{P}(C|I) \quad (\text{S2})$$

The prior distribution of appearance probability parameters W had a simple factorized form

$$\mathbb{P}(W|I) = \prod_i \mathbb{P}(w_{x_i}) \prod_j \mathbb{P}(w_{y_j}) \prod_{j, i \in \text{par}_I(j)} \mathbb{P}(w_{ij}) \quad (\text{S3})$$

where $\text{par}_I(j)$ is the set of chunks that influence (have links to) shape j according to inventory I .

The prior distribution of spatial position parameters had a similar factorized form:

$$\mathbb{P}(C|I) = \prod_i \mathbb{P}(c_{x_i}) \mathbb{P}(\sigma_{x_i}) \prod_j \mathbb{P}(c_{y_j}) \mathbb{P}(\sigma_{y_j}) \prod_{j, i \in \text{par}_I(j)} \mathbb{P}(c_{ij}) \mathbb{P}(\sigma_{ij}) \quad (\text{S4})$$

Table 2 shows the specific distributions used in Eqs. S1-S4.

Sampling the posterior Computing the predictive probability of a test scene $\mathbb{P}(T)$ (Eq. 8) required integration over the joint posterior distribution of inventories and parameters.* This integral was analytically intractable and was thus approximated by a Monte Carlo integral by summing over samples from the posterior distribution. In order to ensure fair sampling, a reversible-jump Markov-chain Monte Carlo (MCMC) sampler (I) was constructed, which was suitable for sampling sub-spaces of different dimensionality, combined with an extended ensemble approach (2), in which Markov-chains were run in parallel at different ‘temperatures’ for better mixing. The integrals were approximated by sums over 500,000 samples collected after having discarded the first 500,000 samples to ensure that the Markov-chain had already attained its stationary distribution.

* Equation 8 formally assumes that participants do not select a single inventory, but rather keep track of the posterior probabilities of *all* possible inventories (Eq. 7) and integrate over this distribution to compute the familiarity (predictive probability) of a scene (model averaging). Another, computationally less extensive alternative would be to concentrate on a *single* inventory, the one with the maximum a posteriori (MAP) probability $\hat{I}_{\text{MAP}} = \text{argmax}_I \mathbb{P}(I|\mathcal{D})$, or the one with maximal marginal likelihood $\hat{I}_{\text{ML}} = \text{argmax}_I \mathbb{P}(\mathcal{D}|I)$ (model selection). We applied the model averaging variant because that gives strictly optimal performance. However, this issue had little practical relevance in our simulations because the posterior over inventories was overwhelmingly dominated by the marginal likelihood of a single inventory, in which case these approaches yield identical results (see also Supporting Text, and Figs. 7-9).

In each iteration of the MCMC sampler the likelihood of an inventory needed to be computed that required computing a sum over x and an integral over u for each scene (Eqs. 4-5). The sum over x was computed by extensively sweeping through all possible 2^H configurations of x , where H is the number of chunks in the inventory. The integral over u was calculated analytically, for each configuration of x , by making use of the fact that the joint distribution of u and v was Gaussian conditioned on x and y due to the model assuming a products of Gaussians form for the process generating spatial positions (Eqs. 2-3). This ensured that the *exact* value of the likelihood could be calculated.

The MATLAB code implementing the sampler is available from the authors upon request.

Associative learner (AL)

Prior distributions The prior distribution of model parameters θ (used for computing the posterior over parameters according to Eq. 7, with I being substituted by θ) was the product of the priors of individual parameters, including appearance and co-appearance parameters w_{y_j} and w_{jk} , absolute and relative spatial position parameters c_{y_j} and c_{jk} , and the corresponding spatial variance parameters σ_{y_j} and σ_{jk} :

$$\mathbb{P}(\theta) = \prod_j \mathbb{P}(w_{y_j}) \mathbb{P}(c_{y_j}) \mathbb{P}(\sigma_{y_j}) \prod_{j,k \geq j} \mathbb{P}(w_{jk}) \mathbb{P}(c_{jk}) \mathbb{P}(\sigma_{jk}) \quad (\text{S5})$$

Table 3 shows the specific distributions used in Eq. S5.

Sampling the posterior Just as the BCL, the AL also required sampling of the posterior (of model parameters θ). Since the number of parameters did not vary, a simpler Metropolis-Hastings MCMC sampler (3) was constructed, combined with extended ensemble techniques (2) for better mixing. The integrals were approximated by sums over 400,000 samples collected after having discarded the first 700,000 samples to ensure that the Markov-chain had already attained its stationary distribution.

The MATLAB code implementing the sampler is available from the authors upon request.

Statistically naïve models (FL, JFL, CPL)

Learning in the frequency learner (FL) amounted to storing the occurrence frequencies of individual shapes during the familiarization phase (see also Table 4). Choice probability of a test scene was calculated by summing the stored frequencies of shapes appearing in the scene and replacing the log predictive probabilities with these sums in Equation 9.[†] This model captured the patterns of experimental data extremely poorly; even the qualitative trends were opposite to those seen in human performance (Fig. 4). Therefore, fitting

[†]Although these models do not define an actual probability distribution over scenes (hence their name ‘statistically naïve’), one can think of the (co)occurrence frequencies learned by the FL (JFL) as playing the role of the canonical parameter of an exponential-family model (such as that used by the AL) that were set to be equal to the sufficient statistic of the model (which is incorrect, in general). In an exponential family model, the probability of a data point (in our case, a scene) is directly related through an exponential function to the negative ‘energy’ of the data point, $\mathbb{P}(x) \propto e^{-E(x)}$, and the negative energy has the form $-E(x) = \sum_i \theta_i f_i(x)$, where $\{\theta_i\}$ is the canonical parameter, and $f_i(x)$ are some functions of x (in our case, each one is a binary indicator of a specific shape(pair) being present in the scene). The sufficient statistic of such a model is $\{\sum_n f_i(x_n)\}$ where x_n is the n th training data point, which in our case is just the counts of (co)occurrences of shapes in the familiarization scenes. Choice probabilities are related to the log probabilities of the test scenes (Eq. 9), which in this case are their negative energies (up to an additive constant that cancels out) that turn out to be just the summed frequencies we used to determine choice probabilities. This gives a formal motivation for the way choice probabilities were computed for these models. A further motivation was direct comparability to previously published results (e.g. see (4,5)) obtained by computing choice probabilities in this way.

parameter β (Eq. 9) would have resulted in uninformative plots ($\beta = 0$ was the trivial solution to minimize squared error) and thus it was fixed at $\beta = 1$ across all experiments.

In the case of the joint frequency learner (JFL) and conditional probability learner (CPL) histograms were built based on the familiarization scenes. One entry of the histogram represented the co-occurrence frequency (JFL) or conditional occurrence frequency (CPL) of a pair of shapes in a given relative spatial position (see also Table 4). Choice probability of a test scene was calculated by summing the entries of the histogram corresponding to all shape pairs present in the scene and replacing the log predictive probabilities with these sums in Equation 9.[†] (Note that the CPL and the AL differ in one crucial aspect: in the CPL, the familiarity of a test scene is only determined by the shapes that are present in it, while in the AL, the absence of shapes is also considered.) In each model, parameter β (see Eq. 9) was fitted for each experiment individually, except for the baseline and frequency-balanced experiments, which were fitted together (so that there were at least two data points to be fitted in each case). A summary of model descriptions can be found in Table 4.

Results

Model fits to human performance

The four experiments of Fig. 2 were fitted with all five models in order to quantitatively evaluate their performance. The summary of the fits of the three statistically naïve models together with the AL and the BCL is shown in Fig. 4. In the baseline experiment, when all combos appeared with equal frequency, all models, except the FL, could reproduce the results obtained with human participants (Fig. 4A). In the frequency-balanced experiment, humans learned the right inventory even though in the familiarization scenes some combos (pairs of shapes) were presented more frequently than others and particular juxtapositions of two frequent pairs appeared just as often as one of the rare pairs. These results ruled out the FL and JFL, which rely on frequency counting, while correlation-based models (CPL and AL) and the BCL showed the same pattern of performance as human learners. In the experiments with combos composed of more than two shapes, naïve statistical learners (FL, JFL, CPL) could only predict identical performance on all test-types, while both the AL and the BCL could well fit human performance (Figs. 4C and D).

Figures 5 and 6 show quantitatively how well the BCL and the AL fitted human performance when both were fit with the same procedure. In each model, parameter β was fitted to data from Experiments 1-4 (red, orange, yellow, and green symbols), and the β value thus obtained was then used to *predict* experimental percent correct values (using again Eq. 9) in the correlation-balanced experiment (blue symbols). (Note that for Figs. 2-3, the AL, but not the BCL, was fit individually for each experiment, see also Methods of the Main Text.) The advantage of the BCL was substantial (compare Figs. 5 and 6) and it was also robust to the particular choice of hyperparameters (compare Figs. 5A and B).

Maximum a posteriori inventories

Learning in the BCL amounted to inferring the posterior probability distribution of inventories (Eq. 7, see also footnote on p.1). However, our numerical simulations showed that familiarization in the experiments was extensive enough so that for each experiment more than 99% of this distribution was concentrated within one inventory (for a formal definition of what constitutes an inventory see Supporting Methods), the maximum a

posteriori (MAP) inventory. Since the prior used for inventories was fairly broad (Table 2), this showed that the posterior was dominated by the marginal likelihoods (Eq. 6).

Analyzing the MAP inventories also gave intuitions as to why the observed patterns emerged in the choice probabilities in the different experiments (Figs. 7-9). In the first four experiments (Fig. 2) the chunks learned by the model corresponded directly to the combos used for constructing the familiarization scenes.

In the frequency-balanced experiment (Figs. 2B and 7B) the chunks’ appearance parameters, w_{x_i} (red numbers in Fig. 7B), reflected the differences in the frequencies of different combos. Therefore, once two chunks for the two frequent pairs had been learned it was not parsimonious to assume an extra combo for their combination if, as in the experiments, each of them also occurred in the absence of the other a number of times. This resulted in low predictive probabilities for mixture pairs composed of shapes belonging to different frequent pairs.

In the triplet and quadruplet experiments (Figs. 2C-D and 8A-B), similar to human performance, the recognition of embedded pairs dropped to close to chance level from the significantly above-chance recognition of true triplets and quadruplets and embedded triplets. This happened because, in the model, the overall predictive probability of an embedded combo was effectively a sum of two terms (the other terms in the sum in Eq. 4 were negligible). One term in the sum expressed the embedded combo as mere ‘noise’, the case when no chunks are present and thus each individual element appears with independent low probabilities (according to its spontaneous appearance parameter, w_{y_j} , blue numbers in Fig. 8). This ‘noise-based’ explanation became increasingly unlikely as the size of the embedded combo grew: shapes appeared independently, the appearance probability of any single one was low, and thus many of them appearing had an exponentially diminishing chance. The other term in the sum expressed the embedded combo as a chunk failing to appear fully. This chunk-based explanation was relatively unlikely since during training combos had always appeared in full, with all of their constituent shapes present. (This almost deterministic relationship was well captured by the high chunk-dependent appearance parameters of the shapes learned in the model, w_{ij} , black numbers in Fig. 8). Because the limiting factor in the chunk-based explanation was the probability of a shape *not* appearing, the predictive probability of an embedded combo did not depend on the size of the embedded combo (the number of shapes that *did* appear), only on the number of shapes of the true combo *not* included in the embedded combo. Thus, in effect, the noise-based account, under which any two combos had the same probability, dominated over the chunk-based account, which could distinguish between a true embedded and a mixture embedded combo, for smaller but not for larger embedded combos.

In the last, correlation-balanced experiment (Figs. 3 and 9), all shapes in the second group-of-4, that were usually shown separately, were assigned to a single common chunk accounting for the scenes in which they were all shown together. Shapes appearing individually were easily accounted for by their spontaneous appearance probabilities (note relatively higher w_{y_j} values, blue numbers, in Fig. 9), therefore it was not parsimonious to introduce extra chunks for each of them separately.

References

1. Green, P.J. Reversible jump MCMC computation and Bayesian model determination. *Biometrika* **82**, 711–732 (1995).
2. Iba, Y. Extended ensemble Monte Carlo. *Int J Mod Phys C* **12**, 623–656 (2001).
3. MacKay, D.J.C. *Information theory, inference, and learning algorithms* (Cambridge University Press, Cambridge, UK, 2003).
4. Fiser, J. & Aslin, R.N. Unsupervised statistical learning of higher-order spatial structures from visual scenes. *Psychol Sci* **12**, 499–504 (2001).
5. Fiser, J. & Aslin, R.N. Encoding multielement scenes: statistical learning of visual feature hierarchies. *J Exp Psychol Gen* **134**, 521–37 (2005).
6. Lee, D.D. & Seung, H.S. Learning the parts of objects by non-negative matrix factorization. *Nature* **401**, 788–791 (1999).

Sigmoid(x)	$= 1 / (1 + \exp(-x))$	$x \in \mathbb{R}$
Bernoulli($x; q$)	$= q^x (1 - q)^{1-x}$	$x \in \{0, 1\}$
Geometric($x; q$)	$= q (1 - q)^x$	$x \in \mathbb{N}$
TruncGeom($x; q, N$)	$= \frac{1}{1-(1-q)^{N+1}} q (1 - q)^x$	$x \in \{0, \dots, N\}$
Exponential($x; \lambda$)	$= \lambda e^{-\lambda x}$	$x \in \mathbb{R}, x \geq 0$
Laplace($x; \mu, b$)	$= \frac{1}{2b} e^{- x-\mu /b}$	$x \in \mathbb{R}$
Normal($x; \mu, \Sigma$)	$= \frac{1}{(2\pi)^{N/2} \Sigma ^{1/2}} e^{-\frac{1}{2} (x-\mu)^\top \Sigma^{-1} (x-\mu)}$	$x \in \mathbb{R}^N$
Dirac-delta($x; \mu$)	$= \prod_{i=1}^N \delta(x_i - \mu_i)$	$x \in \mathbb{R}^N$

Table 1: Functions and distributions used in the text.

Parameter	Prior distribution		Hyperparameters		
			Set 1*	Set 2†	
H	Geometric($H; q$)	q	0.1	0.2	
L	TruncGeom($L; q, H \cdot N$)	q	0.1	0.2	‡
w_{x_i}	Laplace($w_{x_i}; \mu, b$)	μ	0	2	
		b	$\sqrt{2}$	1	
w_{y_j}	Laplace($w_{y_j}; \mu, b$)	μ	-8	-6	
		b	1	$\frac{1}{\sqrt{2}}$	
w_{ij}	Exponential($w_{ij}; \lambda$)	λ	$\frac{1}{6}$	$\frac{1}{3}$	§
c_{x_i}	Dirac-delta($c_{x_i}; \mu$)	μ	[0, 0]	[0, 0]	¶
c_{y_j}	Dirac-delta($c_{y_j}; \mu$)	μ	[0, 0]	[0, 0]	¶
c_{ij}	Normal($c_{ij}; \mu, \Sigma$)	μ	[0, 0]	[0, 0]	¶
		Σ	$2 \cdot \mathbf{I}$	$2\sqrt{2} \cdot \mathbf{I}$	**
σ_{x_i}	Dirac-delta($\sigma_{x_i}; \mu$)	μ	4	$4\sqrt{2}$	**
σ_{y_j}	Dirac-delta($\sigma_{y_j}; \mu$)	μ	4	$4\sqrt{2}$	**
σ_{ij}	Dirac-delta($\sigma_{ij}; \mu$)	μ	$\sqrt{2}$	2	**

Table 2: Parameter priors for the ideal learner. For definitions of probability distributions see Table 1.

Notes:

*Values used for simulations plotted in Figures 2-3, and 5A.

†Values used for simulations plotted in Figure 5B.

‡ N is the number of shapes.

§Non-negativity of link weights was motivated by Ref. 6.

¶The origin [0, 0] was defined as the geometrical center of the grid in which the shapes were presented.

|| \mathbf{I} is the (2×2) identity matrix.

**The unit of spatial coordinates was the length of the edge of a cell in the grid.

Parameter	Prior distribution	
w_{jk}	$\text{Normal}(w_{jk}; 0, 16)$	
w_{y_j}	$\text{Normal}(w_{y_j}; 0, 4)$	
c_{jk}	$\text{Normal}(c_{jk}; [0, 0], 4\mathbf{I})$	*†‡
c_{y_j}	$\text{Normal}(c_{y_j}; [0, 0], 4\mathbf{I})$	*†‡
σ_{ij}	$\text{Exponential}(\sigma_{ij}; 5)$	‡
σ_{y_j}	$\text{Exponential}(\sigma_{y_j}; 1/\sqrt{2})$	‡

Table 3: Parameter priors for the associative learner. For definitions of probability distributions see Table 1.

Notes:

*The origin $[0, 0]$ was defined as the geometrical center of the grid in which the shapes were presented.

† \mathbf{I} is the (2×2) identity matrix.

‡The unit of spatial coordinates was the length of the edge of a cell in the grid.

		FAMILIARIZATION	TEST
FL	single-shape frequency counting	$\text{freq}(\blacktriangleleft), \text{freq}(\blacktriangledown), \text{freq}(\blacksquare) \dots$	$\sum_{\text{for all shapes present}} \text{freq}(\text{shape})$
JFL	shape-pair frequency counting	$\text{freq}(\blacktriangleleft\blacktriangledown), \text{freq}(\blacktriangledown\blacksquare), \text{freq}(\blacksquare\blacktriangleleft) \dots$	$\sum_{\text{for all shape-pairs present}} \text{freq}(\text{shape}_1, \text{shape}_2)$
CPL	shape-pair conditional probabilities	$\text{freq}(\blacktriangleleft\blacktriangledown) / \text{freq}(\blacktriangleleft), \text{freq}(\blacktriangleleft\blacktriangledown) / \text{freq}(\blacktriangledown) \dots$	$\sum_{\text{for all shape-pairs present}} \text{freq}(\text{shape}_1, \text{shape}_2) / \text{freq}(\text{shape}_1)$
AL	probabilistic associative learner	$\text{Prob}(\text{pair-wise correlations} \mid \text{familiarization scenes})$	$\text{Prob}(\text{test scene} \mid \text{pair-wise correlations})$
BCL	Bayesian model comparison	$\text{Prob}(\text{inventory of independent chunks} \mid \text{familiarization scenes})$	$\text{Prob}(\text{test scene} \mid \text{inventory of independent chunks})$

Table 4: Summary of alternative models used to explain human behavior in visual chunk learning experiments. For each model the quantities extracted from familiarization scenes and those used to judge the familiarity of a scene in the test phase of the experiments are shown. The frequency learner (FL) stores single shape occurrence frequencies during familiarization and adds up these frequencies for each shape present in a test scene. The joint frequency learner (JFL) stores co-occurrence frequencies of all possible shape-pairs and adds up these frequencies for each shape-pair present in a test scene. The conditional probability learner (CPL) stores conditional probabilities (co-occurrence frequencies normalized by individual shape frequencies) of all possible (ordered) shape-pairs and adds up these for each shape-pair present in a test scene. The associative learner (AL) infers the strength of associations between all possible pairs of shapes from the familiarization scenes, and based on these computes the probability of a test scene. The Bayesian chunk learner (BCL) infers the probabilities of possible chunk inventories from the familiarization scenes, and based on these computes the probability of a test scene.

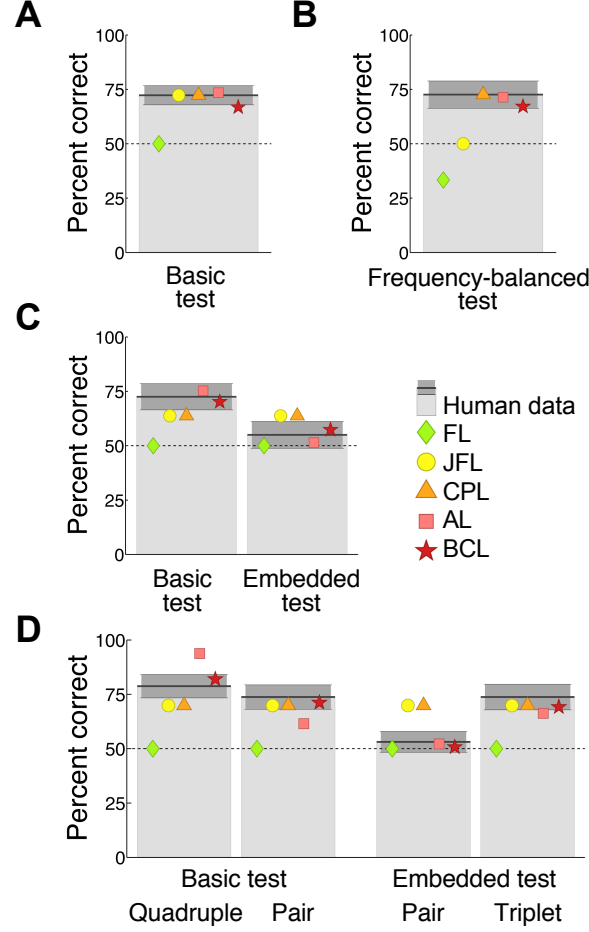


Figure 4: Summary of the performance of the five different models (colored symbols) compared to human performance (gray bars) for a series of experiments from Refs. (4) and (5) using increasingly complex inventories. Models shown are the frequency learner (FL), joint frequency learner (JFL), conditional probability learner (CPL), associative learner (AL), and the Bayesian chunk learner (BCL). Bars indicate average human performance (± 1 standard error of mean, s.e.m.). For a stringent comparison, parameters for the FL, JFL, CPL, and AL models were adjusted independently for each experiment to obtain best fits, whereas the BCL used a single parameter optimization across all experiments. **A**, Inventory containing six equal-frequency pairs. Only the FL failed to predict above-chance human performance on the basic test of true pairs vs. mixture pairs. **B**, Inventory containing six pairs of varying frequencies. The FL and JFL failed to predict above-chance human performance on the test of true rare pairs vs. frequency-balanced mixture pairs. **C**, Inventory containing four equal-frequency triplets. Human performance was above chance on the basic test of true triplets vs. mixture triplets and at chance on the test of embedded pairs vs. mixture pairs. All the statistically naïve models (FL, JFL, CPL) incorrectly predicted equivalent performance on the basic and embedded tests. **D**, Inventory containing two quadruples and two pairs, all with equal frequency. Human performance was above chance on the basic tests of true quadruples or pairs vs. mixture quadruples or pairs, and on the test of embedded triplets vs. mixture triplets, but it was at chance on the test of embedded pairs vs. mixture pairs. Again, the FL, JFL, and the CPL incorrectly predicted the same performance on all tests. Only the AL and the BCL captured the overall pattern of human performance in all these experiments.

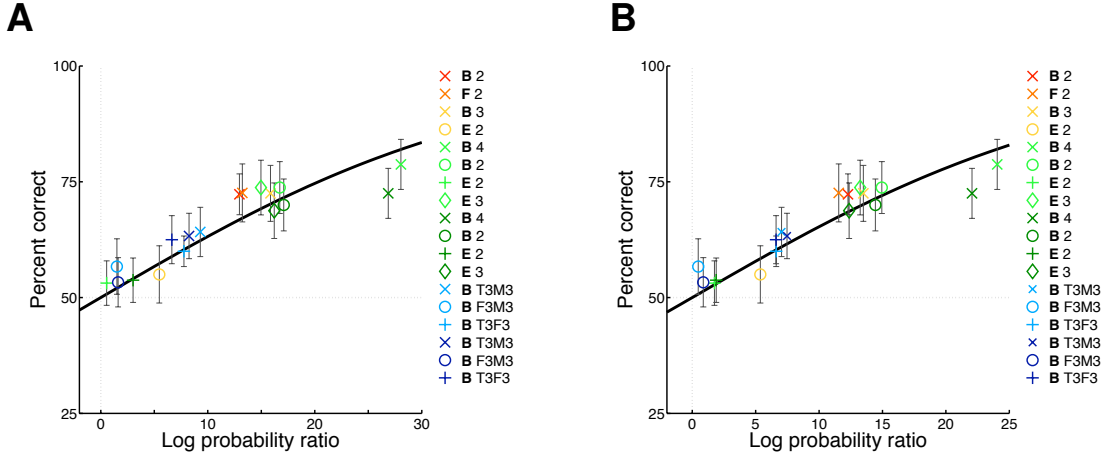


Figure 5: Summary fit of the Bayesian chunk learner (BCL) to human performance. **A**, Simulation results shown in the main text with hyperparameter set 1 (see Supporting Methods and Table 2). **B**, Results of control simulations with hyperparameter set 2 (see Supporting Methods and Table 2) to demonstrate robustness of model predictions to changes in hyperparameters. Each *colored symbol* shows the average percent correct value (\pm s.e.m.) from experimental data for one test type versus the log probability ratio used to determine simulated choice probabilities for the BCL (Eq. 9). *Colors* show experiment type: *red* – baseline experiment (Fig. 2A), *orange* – frequency-balanced experiment (Fig. 2B), *yellow* – triplet experiment (Fig. 2C), *green* – quadruplet experiment (Fig. 2D), *blue* – correlation-balanced experiment (Fig. 3). In the quadruplet and correlation-balanced experiments a group of participants were trained on the first half of the familiarization scenes and were tested after this limited training: *dark colors* – mid-familiarization test results, *light colors* – test results after completion of the familiarization phase (data plotted in Figs. 2D and 3B). *Letters* denote test type (Fig. 2, middle row): *B* – baseline test, *F* – frequency-balanced test, *E* – embedded test; in the correlation-balanced experiment: *T3M3* – true triplet versus mixture triplet test, *F3M3* – false triplet versus mixture triplet test, *T3F3* – true triplet versus false triplet test (see Fig. 3B). *Numbers* denote size of test combo: 2 – pair, 3 – triplet, 4 – quadruplet. *Thick black line* is the predicted choice probability of the BCL (Eq. 9) after fitting $\beta = 0.054$ (**A**) and $\beta = 0.063$ (**B**). The correlation (Pearson’s correlation coefficient) between experimental data and model predictions is $r = 0.88$ ($p < 0.0002$) (**A**) and $r = 0.89$ ($p < 0.0001$) (**B**) for data used for fitting the model (red, orange, yellow, and green symbols), and $r = 0.92$ ($p < 0.006$) (**A**) and $r = 0.92$ ($p < 0.009$) (**B**) for predicted data (blue symbols). See also Methods of the Main Text and Supporting Text for details of the fitting procedure.

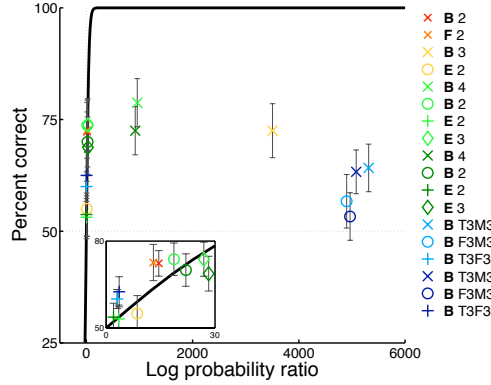
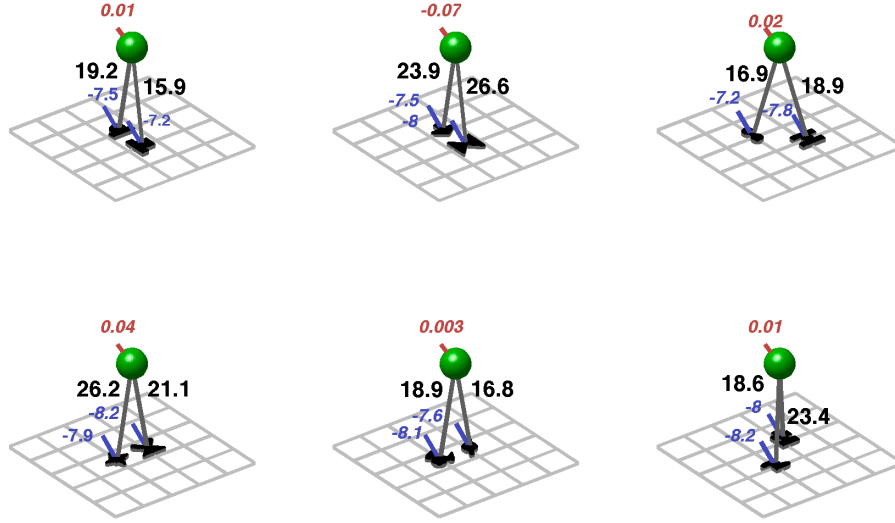


Figure 6: Summary fit of the associative learner (AL) to human performance. Each *colored symbol* shows the average percent correct value (\pm s.e.m.) from experimental data for one test type versus the log probability ratio used to determine simulated choice probabilities for the AL (Eq. 9). *Inset* shows magnified area of the graph. *Colors* show experiment type: *red* – baseline experiment (Fig. 2A), *orange* – frequency-balanced experiment (Fig. 2B), *yellow* – triplet experiment (Fig. 2C), *green* – quadruplet experiment (Fig. 2D), *blue* – correlation-balanced experiment (Fig. 3). In the quadruplet and correlation-balanced experiments participants were also tested after half of the familiarization scenes had been shown: *dark colors* – mid-familiarization test results, *light colors* – test results after completion of the familiarization phase (data plotted in Figs. 2D and 3B). *Letters* denote test type (Fig. 2, middle row): *B* – baseline test, *F* – frequency balanced test, *E* – embedded test; in the correlation-balanced experiment: *T3M3* – true triplet versus mixture triplet test, *F3M3* – false triplet versus mixture triplet test, *T3F3* – true triplet versus false triplet test (see Fig. 3B). *Numbers* denote size of test combo: 2 – pair, 3 – triplet, 4 – quadruplet. *Thick black line* is the predicted choice probability of the AL (Eq. 9) after fitting $\beta = 0.042$. The correlation (Pearson’s correlation coefficient) between experimental data and model predictions is $r = 0.71$ ($p < 0.01$) for data used for fitting the model (red, orange, yellow, and green symbols), and $r = -0.23$ ($p > 0.65$) for predicted data (blue symbols). See also Methods of the Main Text and Supporting Text for details of the fitting procedure.

A



B

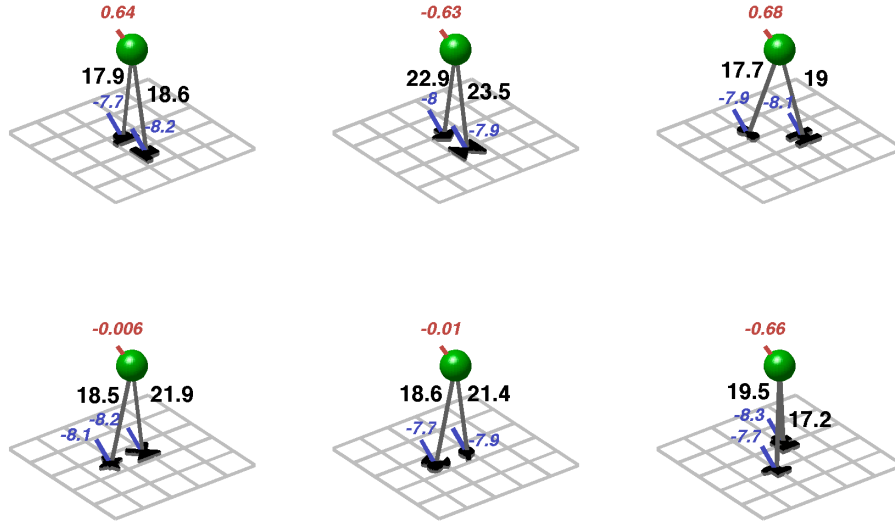
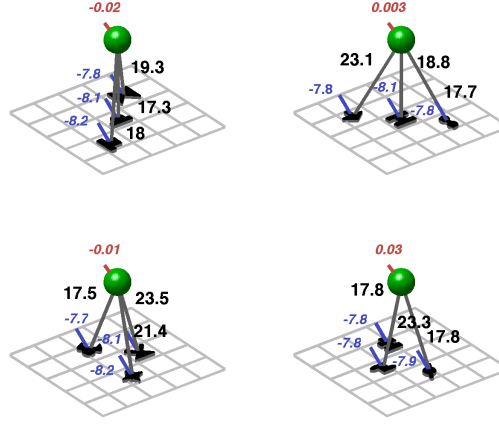


Figure 7: Maximum a posteriori (MAP) inventories, and posterior means of the parameters within the MAP inventories, learned by the BCL in the baseline (**A**, Fig. 2A) and frequency-balanced experiments (**B**, Fig. 2B). Each panel shows the parameters belonging to a chunk (*green sphere*) and to the *shapes* it influences. The tilted grid shows the grid used in the visual scenes for reference. The position of the green sphere (along the grid) shows the spatial position parameter $c_{x_i} = [0, 0]$ of the chunk (fixed without learning), and the *red number* shows its appearance parameter, w_{x_i} . The positions of the *shapes* in the grid show their relative spatial position parameters, c_{ij} , and the *blue numbers* and *black numbers* show their ‘spontaneous’ and chunk-dependent appearance parameters, w_{y_j} and w_{ij} , respectively.

A



B

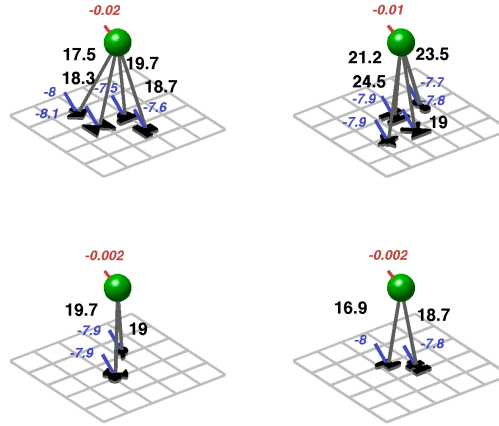


Figure 8: Maximum a posteriori (MAP) inventories, and posterior means of the parameters within the MAP inventories, learned by the BCL in the triplet (**A**, Fig. 2C) and quadruplet experiments (**B**, Fig. 2D). Each panel shows the parameters belonging to a chunk (*green sphere*) and to the *shapes* it influences. The tilted grid shows the grid used in the visual scenes for reference. The position of the green sphere (along the grid) shows the spatial position parameter $c_{x_i} = [0, 0]$ of the chunk (fixed without learning), and the *red number* shows its appearance parameter, w_{x_i} . The positions of the *shapes* in the grid show their relative spatial position parameters, c_{ij} , and the *blue numbers* and *black numbers* show their ‘spontaneous’ and chunk-dependent appearance parameters, w_{y_j} and w_{ij} , respectively.

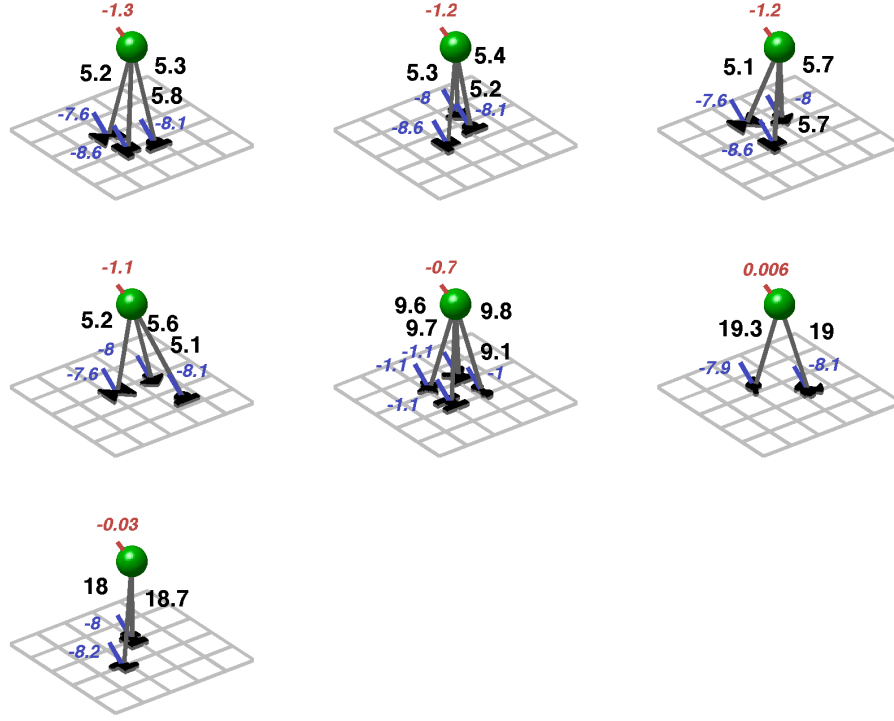


Figure 9: Maximum a posteriori (MAP) inventories, and posterior means of the parameters within the MAP inventories, learned by the BCL in the correlation-balanced experiment (Fig. 3). Each panel shows the parameters belonging to a chunk (*green sphere*) and to the *shapes* it influences. The tilted grid shows the grid used in the visual scenes for reference. The position of the green sphere (along the grid) shows the spatial position parameter $c_{x_i} = [0, 0]$ of the chunk (fixed without learning), and the *red number* shows its appearance parameter, w_{x_i} . The positions of the *shapes* in the grid show their relative spatial position parameters, c_{ij} , and the *blue numbers* and *black numbers* show their ‘spontaneous’ and chunk-dependent appearance parameters, w_{y_j} and w_{ij} , respectively.